



Studies on spray deposited Ni doped Mn₃O₄ electrodes for supercapacitor applications

A.G. Naiknaware, J.U. Chavan, S.H. Kaldate, Abhijit A. Yadav*

Thin Film Physics Laboratory, Department of Physics, Electronics and Photonics, Rajarshi Shahu Mahavidyalaya, (Autonomous) Latur, 413512, Maharashtra, India

ARTICLE INFO

Article history:

Received 1 July 2018

Received in revised form

29 September 2018

Accepted 1 October 2018

Available online 2 October 2018

Keywords:

Chemical synthesis

Structural properties

FESEM

Supercapacitors

Energy storage

ABSTRACT

The doping influenced morphological alteration and its consequent impact on electrochemical properties of Mn₃O₄ electrodes has been investigated. The Ni doped Mn₃O₄ are characterized for its surface morphological, compositional, structural, optical and electrochemical properties. The polycrystalline nature of Ni doped Mn₃O₄ films with tetragonal Hausmannite crystal structure has been confirmed from x-ray diffraction. The field emission scanning electron microscope study shows that Ni doped Mn₃O₄ films have porous nanoflakes type surface morphology. The band gap energy for Ni doped Mn₃O₄ films ranges between 2.55 and 3.29 eV depending on the Ni doping. The specific capacitance of 705 Fg⁻¹ from cyclic voltammetry and 740 Fg⁻¹ from galvanostatic charge/discharge has been perceived. The Ni doped Mn₃O₄ electrode show good electrochemical cycling stability. The electrochemical impedance study showed charge transfer resistance of 6.8 Ωcm² for 0.50 mol % Ni doped Mn₃O₄ electrode.

© 2018 Elsevier B.V. All rights reserved.

1. Introduction

The production and storage of energy is a most imperative theme of Todays discussion in research. The rising prices and pollution are among the difficulties associated with the dependency of society on fossil fuels [1,2]. Throughout the last decade, many attempts are done to discover ecological and reproducible energy storage devices [3–6]. Among the storage technologies, supercapacitors have drawn excessive consideration due to longer cycle life than batteries, greater power density and more energy density as compared to conventional capacitors [7,8]. In certain applications requiring the low energy and high power density, supercapacitors have underway to substitute the batteries [9–12].

Supercapacitors are categorized in two sets based on their charging mechanism, namely (i) EDLCs and (ii) pseudocapacitors [13–15]. The supercapacitor performance hangs on the chemical and physical properties of the electrode. Recently, transition metal oxides, including NiO, SnO₂, Co₃O₄, RuO₂, Fe₂O₃, MnO₂, Fe₃O₄, ZnO and Mn₃O₄ have been considered as candidates for supercapacitor electrodes [16–21]. Amongst these, Mn₃O₄ with benefits of little cost, effective semiconducting nature and ecofriendly has been functional widely.

The doped and pure Mn₃O₄ films can be deposited by numerous techniques comprising atomic layer deposition [22], sputtering [23], co-precipitation [24], SILAR [25], chemical synthesis [26], sol-gel method [27], electrodeposition [28], hydrothermal method [29–31] and spray pyrolysis [15,21,32–35]. Amongst these, spray pyrolysis technique has little cost, straightforward and simple to use, has been recognized for number of scientific studies and technical applications.

Adjusting the morphology of the electrodes is significant in the context of Mn₃O₄ because each structure has its own merits when used in a potential application such as catalyst, sensor, rechargeable batteries, supercapacitors etc [16–18]. Recently it has been shown that catalytic, electronic and optical properties of Mn₃O₄ electrodes are highly reliant on their morphologies and crystallographic forms [31–34]. Previously, we have reported porous Mn₃O₄ thin films with tetragonal Hausmannite crystal structure. The specific capacitance of 394 Fg⁻¹ was observed. Although a considerable improvement in the electrochemical performance has been noted [15], the observed specific capacitance is smaller compared with the existing literature, which can be attributed partially to the greater resistivity of the electrode that might be lowered by adding appropriate donor impurity. It is reported that appropriate doping can disturb the growth process during chemical reaction and therefore the morphology of the metal oxide can be altered by varying the doping concentration. So suitable doping can be a good

* Corresponding author.

E-mail address: ay_physics@yahoo.co.in (A.A. Yadav).



way to change the morphology of Mn_3O_4 . Among the different doping materials, Ni can be a good dopant for Mn_3O_4 , as the ionic radii of Mn (0.80 \AA) and Ni (0.72 \AA) are comparable [36] and Ni had been successfully doped in manganese tetraoxide thin films previously. Nickel doping in Mn_3O_4 is a real approach to enhance the performance of Mn_3O_4 supercapacitor. The influence Ni doping on morphological, compositional, structural, optical and electrochemical properties of Mn_3O_4 thin films has been investigated.

2. Experimental

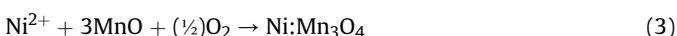
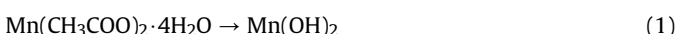
Ni doped Mn_3O_4 electrodes are deposited at various Ni concentrations. For deposition of Ni doped Mn_3O_4 electrodes manganese acetate ($\text{Mn}(\text{CH}_3\text{COO})_2 \cdot 4\text{H}_2\text{O}$) and Nickel chloride hexahydrate ($\text{NiCl}_2 \cdot 6\text{H}_2\text{O}$) were used. The optimized preparative parameters used for deposition were: concentration of manganese acetate 0.8 M ; deposition temperature 350°C ; spray rate $3\text{--}4 \text{ cm min}^{-1}$; carrier gas pressure 1.8 kg cm^{-2} ; substrate to nozzle distance 28 cm ; Ni doping concentration $0\text{--}1 \text{ mol \%}$ and glass and FTO coated glass as substrates. For each deposition, 25 ml 0.8 M $[\text{Mn}(\text{CH}_3\text{COO})_2 \cdot 4\text{H}_2\text{O}]$ solution was mixed with 25 ml of Propan-2-ol to make the final spraying solution of 50 ml . The resulting concentration of spraying solution (50 ml) was 0.4 M . The Ni doping concentration was varied from 0 to 1 mol \% by keeping all other parameters at optimized values and films were deposited by using computerized chemical spray pyrolysis technique discussed elsewhere [37].

Structural characterization of Ni doped Mn_3O_4 electrodes was performed by examining the X-ray diffraction (XRD) patterns obtained through Philips X-ray diffractometer model PW-1710 ($\lambda = 1.54060 \text{ \AA}$ for $\text{Cu-K}\alpha$ radiation) within 2θ between 20 and 80° . Surface morphological and compositional studies were performed using JEOL JSM-6360, Mira-3, Tescan, Brno-Czech Republic, field emission scanning electron microscope (FESEM) at accelerating voltage of 20 kV . The absorption spectrum of Ni doped Mn_3O_4 was recorded through Systronic make UV-Vis Spectrophotometer (model 119). The absorption data was used to decide the type of transition and band gap.

The electrochemical performance was tested in a standard three-electrode cell on a CHI 660E, (CH Instruments, USA), with Ni doped Mn_3O_4 -working electrode, Platinum foil-counter electrode, and Ag/AgCl-reference electrode. An aqueous 1 M Na_2SO_4 electrolyte was utilised. Cyclic voltammetry (CV) investigation was performed in 0.25 to $+0.45 \text{ V}$ versus Ag/AgCl at various scan rates. The galvanostatic charging/discharging was conducted at different current densities (0.5 A g^{-1} to 4 A g^{-1}) inside a potential window of -0.2 to $+0.4 \text{ V}$. The electrochemical impedance spectroscopy measurement was accomplished at AC amplitude of 5 mV in 100 kHz - 1Hz frequency range.

3. Results and discussion

The solution of manganese acetate ($\text{Mn}(\text{CH}_3\text{COO})_2 \cdot 4\text{H}_2\text{O}$) in aqueous/organic solvent mixture provides Mn^{2+} ions, the chemical reaction between Mn^{2+} and 2OH^- leads to formation of $\text{Mn}(\text{OH})_2$, which is then decomposed into MnO . At optimum substrate temperature, oxidation of MnO by atmospheric oxygen leads to the formation of the adherent Mn_3O_4 layer. The Nickel chloride hexahydrate ($\text{NiCl}_2 \cdot 6\text{H}_2\text{O}$) provides the Ni ions. The reaction can be written as [38],



The mass of Ni doped Mn_3O_4 electrodes are measured by using sensitive microbalance. It is observed that the masses for all samples were in the range of $0.54 \pm 0.03 \text{ mg cm}^{-2}$.

3.1. X-ray diffraction (XRD)

Fig. 1 displays XRD pattern of Ni doped Mn_3O_4 films deposited with various Ni concentrations. The angle 2θ is between 20 and 80° . XRD pattern represents polycrystalline Ni doped Mn_3O_4 with tetragonal Hausmannite crystal structure as accorded with standard JCPDS data card 75–1560. The prominent diffraction peaks are observed at $2\theta = 24.45^\circ, 29.13^\circ, 32.50^\circ, 36.32^\circ, 38.69^\circ, 44.45^\circ, 52.01^\circ, 60.15^\circ$, and 64.90° corresponding to hkl planes $(112), (202), (220), (213), (004), (400), (332), (404)$, and (440) respectively. The observed diffraction peak positions in Ni doped Mn_3O_4 films were matching with earlier results [33,34]. As seen from **Fig. 1** and **Table 1**, the peak positions of the Ni incorporated Mn_3O_4 thin films with various Ni doping were closely identical to those of bulk Mn_3O_4 , manifesting the same Hausmannite lattice structure [15].

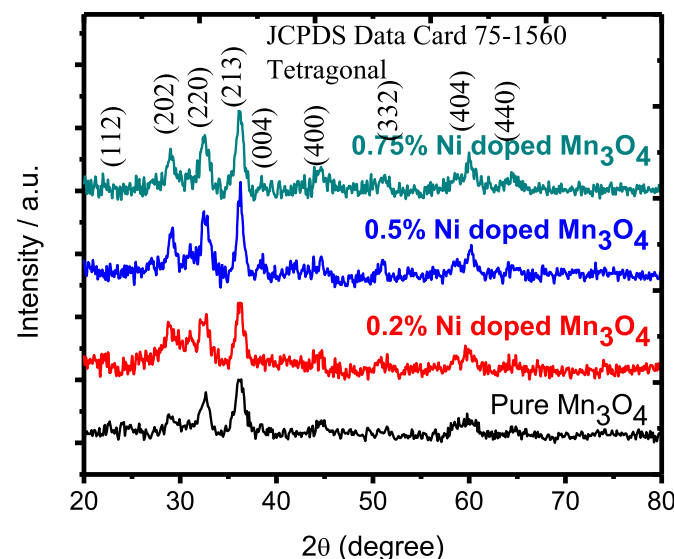


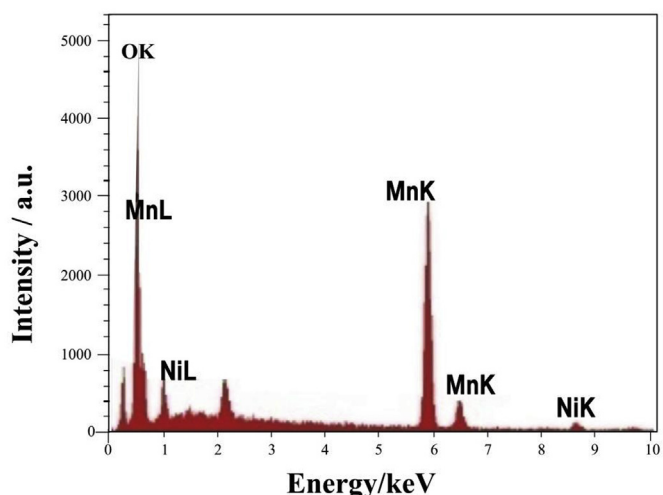
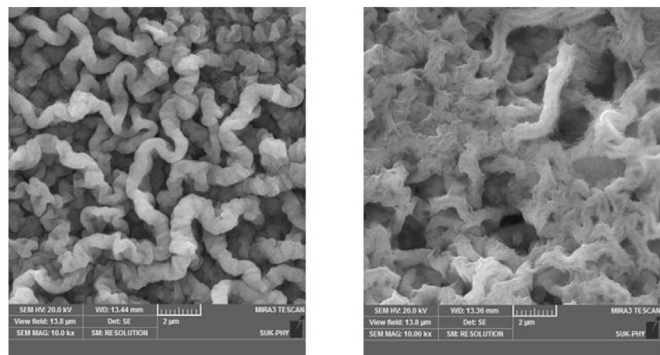
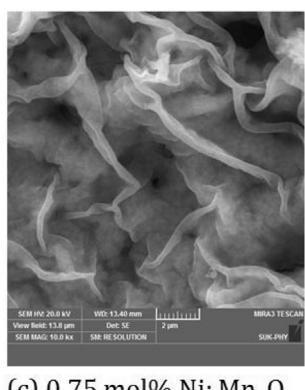
Fig. 1. XRD Patterns of spray deposited Ni doped Mn_3O_4 thin films.

Table 1
XRD data for spray deposited Ni doped Mn_3O_4 thin films.

| Ni doping (mol%) | $2\theta^\circ$ | d (Å) calculated | d (Å) | Assignment standard | Crystalline size (nm) |
|------------------|-----------------|------------------|-------|---------------------|-----------------------|
| 0 | 25.14 | 3.539 | 3.645 | 112 | |
| | 29.20 | 3.056 | 3.079 | 202 | |
| | 32.67 | 2.738 | 2.878 | 220 | |
| | 36.34 | 2.470 | 2.377 | 213 | 39 |
| | 38.12 | 2.359 | 2.355 | 004 | |
| | 44.35 | 2.041 | 2.035 | 400 | |
| | 50.98 | 1.790 | 1.777 | 332 | |
| | 60.10 | 1.538 | 1.540 | 404 | |
| | 64.85 | 1.436 | 1.439 | 440 | |
| | 24.37 | 3.649 | 3.645 | 112 | |
| 0.20 | 29.07 | 3.069 | 3.079 | 202 | |
| | 32.76 | 2.731 | 2.878 | 220 | |
| | 36.39 | 2.467 | 2.377 | 213 | 40 |
| | 39.58 | 2.275 | 2.355 | 004 | |
| | 44.74 | 2.024 | 2.035 | 400 | |
| | 51.54 | 1.772 | 1.777 | 332 | |
| | 60.21 | 1.536 | 1.540 | 404 | |
| | 64.86 | 1.436 | 1.439 | 440 | |

Table 1 (continued)

| Ni doping (mol%) | $2\theta(^{\circ})$ | d (Å) calculated | d (Å) | Assignment standard | Crystalline size (nm) |
|------------------|---------------------|------------------|-------|---------------------|-----------------------|
| 0.50 | 24.47 | 3.634 | 3.645 | 112 | 42 |
| | 29.25 | 3.050 | 3.079 | 202 | |
| | 32.47 | 2.755 | 2.878 | 220 | |
| | 36.29 | 2.473 | 2.377 | 213 | |
| | 38.61 | 2.330 | 2.355 | 004 | |
| | 44.76 | 2.023 | 2.035 | 400 | |
| | 52.21 | 1.750 | 1.777 | 332 | |
| | 60.27 | 1.534 | 1.540 | 404 | |
| | 64.76 | 1.438 | 1.439 | 440 | |
| | 23.83 | 3.731 | 3.645 | 112 | |
| 0.75 | 29.02 | 3.074 | 3.079 | 202 | 41 |
| | 32.10 | 2.786 | 2.878 | 220 | |
| | 36.27 | 2.474 | 2.377 | 213 | |
| | 38.48 | 2.337 | 2.355 | 004 | |
| | 43.95 | 2.058 | 2.035 | 400 | |
| | 53.33 | 1.716 | 1.777 | 332 | |
| | 60.03 | 1.540 | 1.540 | 404 | |
| | 65.14 | 1.431 | 1.439 | 440 | |

**Fig. 3.** EDS pattern of 0.5 mol% Ni doped Mn_3O_4 thin films.**(a) 0.2 mol% Ni: Mn_3O_4** **(b) 0.5 mol% Ni: Mn_3O_4** **(c) 0.75 mol% Nickel: Mn_3O_4** **Fig. 2.** FESEM images of Ni doped Mn_3O_4 thin films (a) 0.2 mol%, (b) 0.5 mol%, and (c) 0.75 mol% Nickel, respectively at 10,000 \times magnifications.

No other crystalline phases were detected in any of the XRD patterns. This demonstrated that Ni doping did not affect the original crystalline structure.

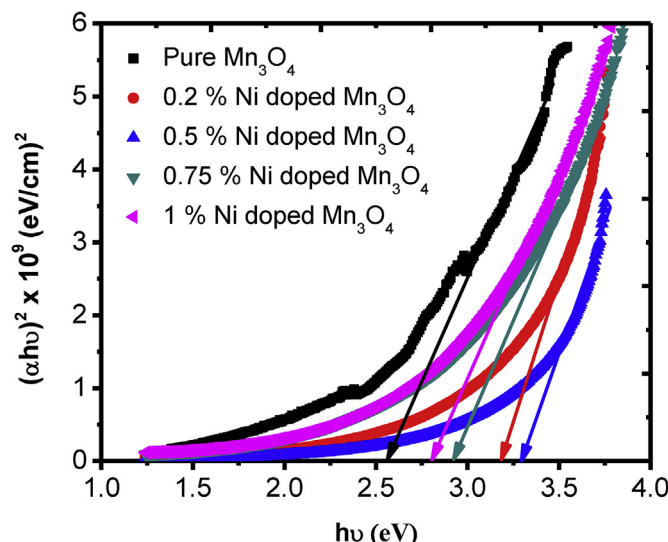
In addition, Ni doped Mn_3O_4 films are greatly oriented along (213) direction. It is witnessed that the peak (213) intensity augmented with increase Ni doping concentrations upto 0.50 mol% and decreases thereafter showing slight reorientation effect. The probable reason for such behavior is that the nickel atom alternates with manganese up to 0.5 mol% while for higher nickel doping

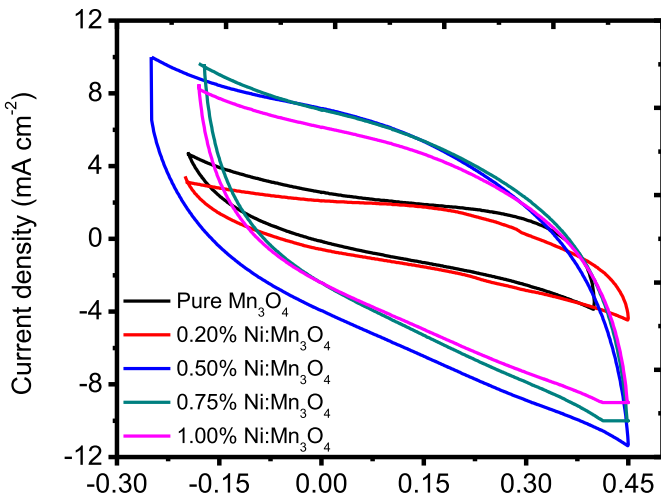
(>0.5 mol%), nickel atoms go to substitutional as well as interstitial positions of Mn_3O_4 lattice [15]. The lattice parameters calculated using the standard relation [15] are found to be, $a = b = 8.135 \text{ \AA}$, $c = 9.28 \text{ \AA}$; which are closely matching with standard ($a = b = 8.14 \text{ \AA}$, $c = 9.42 \text{ \AA}$) of Mn_3O_4 thin films (JCPDS card 75–1560).

Crystalline size is calculated for the standard (213) reflection using Scherrer's formula [39]. The FWHM decrease initially with increase in nickel doping in Mn_3O_4 up to 0.50 mol% and further found to increase with further increase in nickel doping. Crystalline size is found in between 39 and 42 nm for Ni doped Mn_3O_4 with various nickel doping. Table 1 depicts 2θ , interplanar spacing (d), assignments and crystalline size for Ni doped Mn_3O_4 .

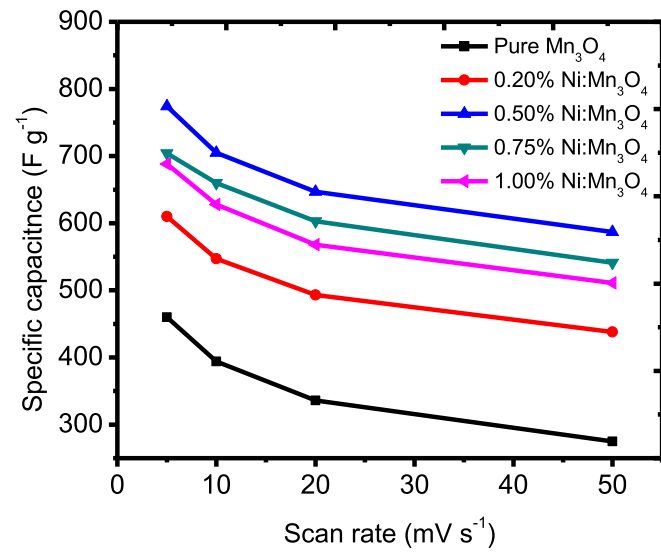
3.2. Field emission scanning electron microscopy (FESEM) and energy-dispersive X-ray spectroscopy (EDS)

The modifications in surface morphology of the Ni incorporated Mn_3O_4 are presented in Fig. 2. The surface of undoped Mn_3O_4 thin film was observed as porous with densely packed and well adhered to

**Fig. 4.** Plot of $(\alpha h\nu)^2$ versus $h\nu$ for Ni doped Mn_3O_4 thin films.



(a)



(b)

Fig. 5. (a) The CVs of Ni doped Mn_3O_4 thin film electrodes in the 1 M Na_2SO_4 electrolyte, at scan rate of 10 mVs^{-1} ; (b) Specific capacitance vs. scan rate for Ni doped Mn_3O_4 electrodes with various Ni doping.

the substrate [15]. Fig. 2 shows the FESEM images of Ni doped Mn_3O_4 deposited with 0.2 mol %, 0.5 mol % and 0.75 mol % nickel concentrations at $10,000 \times$ magnifications. From figure it is seen that Ni doped Mn_3O_4 show the porous nanoflakes type surface morphology. After Nickel doping, the Mn_3O_4 thin film is transformed into highly porous nanoflakes, as seen in Fig. 2(a–c). Such porous nanoflakes afford a much larger surface area needed for supercapacitors [40,41]. The porosity is witnessed to enhance with the increase in nickel doping upto 0.50 mol%, influencing the electrochemical property. Similar transformations in morphology of the Mn_3O_4 thin film electrodes were also found in previous studies [42].

The doping of Ni in the Mn_3O_4 electrode was confirmed by energy-dispersive X-ray spectroscopy (EDS). Fig. 3 shows strong peak signals of only Mn, O, and Ni components of the 0.5 mol% Ni doped Mn_3O_4 electrode, approving incorporation of Ni in Mn_3O_4 lattice.

Table 2

Optical and electrochemical (CV) data for spray deposited Ni doped Mn_3O_4 thin films.

| Ni doping (mol %) | E_g (eV) | C_{sp} Fg^{-1} | $R_s(\Omega)$ | $R_{ct}(\Omega \text{cm}^2)$ |
|-------------------|------------|---------------------------|---------------|------------------------------|
| 0.00 | 2.55 | 394 | 0.50 | 11.70 |
| 0.20 | 3.15 | 547 | 0.35 | 10.20 |
| 0.50 | 3.29 | 705 | 0.25 | 6.80 |
| 0.75 | 2.87 | 660 | 0.32 | 8.25 |
| 1.00 | 2.80 | 628 | 0.33 | 10.00 |

E_g : bandgap energy, C_{sp} : specific capacitance at scan rate of 10 mVs^{-1} , R_s : solution resistance, R_{ct} : charge transfer resistance.

3.3. Optical

Optical characterization of Ni doped Mn_3O_4 electrodes were carried out by measuring the absorption spectra in the wavelength span of 300–1100 nm. From absorption spectra (not shown here), it is observed that the absorption edge marginally moved to shorter wavelengths with nickel doping up to 0.5 mol% showing dependence of absorbance on impurity addition [34,43]. The absorption spectra was further analysed to decide the type of transition and band gap energy by plotting a graph of $(\alpha h\nu)^2$ versus $h\nu$ as shown in Fig. 4. The absorption coefficient is in range of 10^4 cm^{-1} . The nature of the plots designates the direct allowed type transition. The band gap energy obtained by extrapolating the $(\alpha h\nu)^2$ versus $h\nu$ curves is found to be in between 2.55 and 3.29 eV. The bandgap upsurges with increase in Ni doping in Mn_3O_4 ion, reaches a maximum value 3.29 eV at 0.50 mol% and further decreases with Ni doping. The upsurge in bandgap of Ni incorporated Mn_3O_4 thin films can be accredited to the presence of holes formed by nickel ions substituting manganese ions in the host lattice [44]. The band gap energy of 2.55–3.29 eV obtained in present case is comparable with 2.23–2.82 eV reported for Li doped Mn_3O_4 by Amara et al. [44], 2.20–2.92 eV reported for spray deposited Zr doped Mn_3O_4 thin films by Said and coworkers [34], and 2.6–2.8 eV for thallium doped Mn_3O_4 by Sheikhshoaei et al. [27].

3.4. Electrochemical

3.4.1. Cyclic voltammetry (CV)

Fig. 5 (a) shows the cyclic voltammograms of Ni doped Mn_3O_4

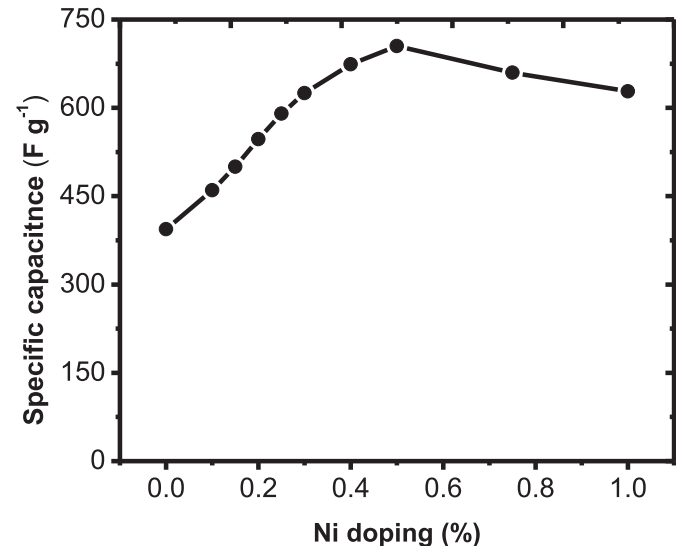
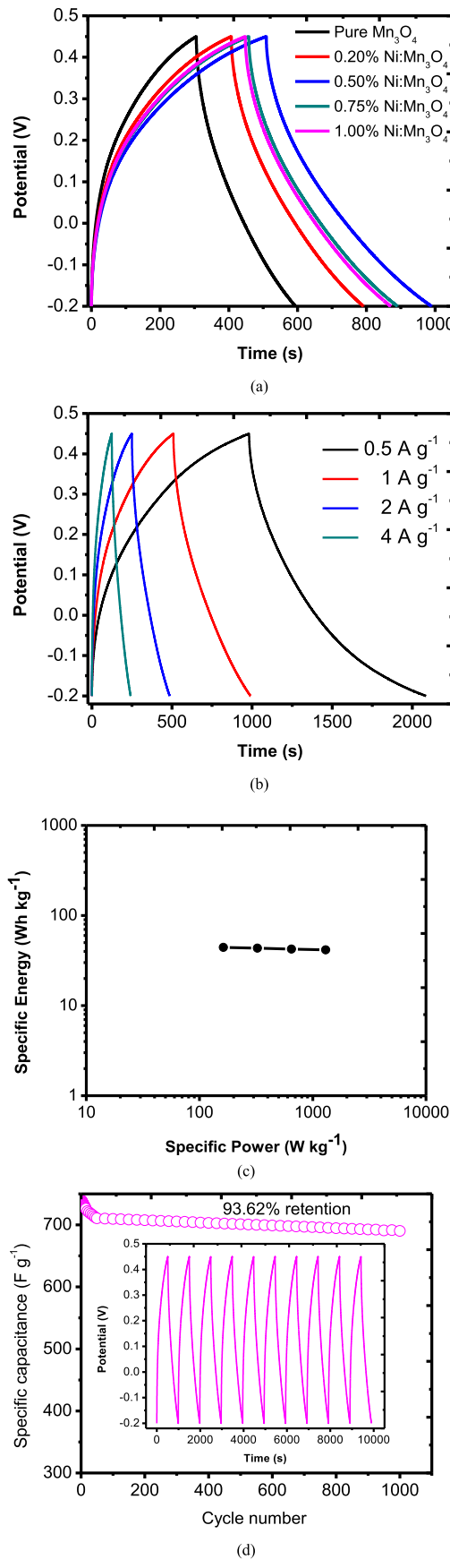


Fig. 6. Variation of the specific capacitance (10 mVs^{-1}) with Ni doping in Mn_3O_4 thin films.

**Table 3**

Various parameters for obtaining specific capacitance (C_s), specific energy (SE) and specific power (SP) from GCD.

| CD (Ag^{-1}) | t_{dis} (s) | C_s Fg^{-1} | SE (Whkg^{-1}) | SP (Wkg^{-1}) | η (%) |
|-------------------------|----------------------|------------------------|---------------------------|--------------------------|------------|
| 0.5 | 981 | 755 | 44.28 | 162.5 | 95.71 |
| 1 | 481 | 740 | 43.42 | 325 | 94.69 |
| 2 | 235 | 723 | 42.43 | 650 | 93.25 |
| 4 | 115 | 708 | 41.53 | 1300 | 92.74 |

CD; current density, t_{dis} ; discharge time, η ; coulomb efficiency.

electrode (3 electrode assembly) at scan rate 10 mVs^{-1} in $1 \text{ M Na}_2\text{SO}_4$ electrolyte within potential -0.25 to $+0.45 \text{ V}$ versus Ag/AgCl . The regular and symmetric shapes of CV curves prove the typical pseudo-capacitive performance. The specific capacitance of Ni doped Mn_3O_4 electrodes was calculated from CV curves using relation given elsewhere [15]. The specific capacitances of Ni doped Mn_3O_4 electrodes are given in Table 2.

Furthermore, Ni doped Mn_3O_4 electrodes show good rate capability (Fig. 5. (b)) with specific capacitance of 705 Fg^{-1} (at 10 mVs^{-1}) for 0.5 mol \% Ni doping, which is greater than the specific capacitance reported for Zinc Oxide/Manganese Oxide [45]. From Fig. 5 (b), the specific capacitances of all the samples decrease with growing scan rates. This is ascribed to the presence of inner active sites, which completely inhibit the redox transitions at higher scan rates of CV, probably owing to the diffusion effect of protons within the electrodes. All the electrodes showed the maximum specific capacitance at a scan rate of 5 mVs^{-1} . It is witnessed that the capacitance enhances with incorporation of Ni in Mn_3O_4 with a maximum 705 Fg^{-1} for 0.5 mol \% and diminishing thereafter for further incorporation of Ni in Mn_3O_4 . This can be ascribed to porous nanoflakes type morphology of Ni doped Mn_3O_4 thin film at 0.50 mol \% , which gives more surface wetting for Na_2SO_4 electrolyte with Mn_3O_4 electrode [46]. The specific capacitance of 705 Fg^{-1} witnessed in present study is better than 263 Fg^{-1} reported for $\text{Mn}_3\text{O}_4/\text{Ni}$ foam prepared facile one-step hydrothermal method [47] and 430 Fg^{-1} at 5 mVs^{-1} for $\text{MnO}_2\text{-RuO}_2@\text{GNR}$ electrode [48]. The large specific capacitance is accredited to the nanoflake type porous morphology of Ni doped Mn_3O_4 electrodes observed from FESEM (Fig. 2). Fig. 6 shows behavior of specific capacitance with Ni incorporation in Mn_3O_4 . Even though the specific capacitance of undoped and nickel doped Mn_3O_4 are comparable to those of familiar existing carbon-based capacitors, undoped and nickel doped Mn_3O_4 are of considerable attention owing to their comparatively easy synthesis, low cost, and environment friendliness.

3.4.2. Galvanostatic charge/discharge (GCD)

To determine the voltage stability window of nickel doped Mn_3O_4 , GCDs (Fig. 7a) were carried out at 1 Ag^{-1} in a steady potential window -0.2 to $+0.4 \text{ V}$. Fig. 7a shows that the GCD curves for nickel incorporated Mn_3O_4 electrodes. The nature of curves confirms the pseudo-capacitive behavior of nickel incorporated Mn_3O_4 electrodes. The discharge curve of the electrodes involves of two portions: an IR drop owing to internal resistance and a capacitive component (curved portion) related to the voltage change due to changes in energy within the capacitor [49]. This (IR)

Fig. 7. (a) GCD curves for Ni doped Mn_3O_4 electrodes at fixed current density of 1 Ag^{-1} , (b) GCD curves for 0.5 mol \% Ni doped Mn_3O_4 electrode at different current densities, (c) Ragone plots for 0.5 mol \% Ni doped Mn_3O_4 thin film electrode supercapacitor, and (d) cycling performance of the 0.5 mol \% Ni doped Mn_3O_4 electrode at current density of 1 Ag^{-1} . The inset shows the charge/discharge curves of the first 10 cycles.

Table 4

The capacitive performance comparison of pure and doped Mn_3O_4 by this work with various manganese oxide reported in some literatures.

| Order | Material | Electrolyte | Measurement Protocol | Max.capacitance | Ref. |
|-------|----------------------------------|--------------------------------|------------------------------|-----------------------|------|
| 1 | Sn-doped Mn_3O_4 | 6 M KOH | GCD = 5 A g^{-1} | 216 F g^{-1} | [52] |
| 2 | Ni-doped Mn_3O_4 | 0.5 M Na_2SO_4 | GCD = 0.25 A g^{-1} | 230 F g^{-1} | [50] |
| 3 | Ni-doped Mn_3O_4 | 1 M KOH | GCD = 1 A g^{-1} | 707 F g^{-1} | [53] |
| 4 | Ni-doped Mn_3O_4 | 1 M KOH | GCD = 1 A g^{-1} | 407 F g^{-1} | [54] |
| 5 | Ce-doped Mn_3O_4 | 1 M Na_2SO_4 | GCD = 2 A g^{-1} | 209 F g^{-1} | [55] |
| 6 | Cr-doped Mn_3O_4 | 1 M Na_2SO_4 | GCD = 0.5 A g^{-1} | 272 F g^{-1} | [30] |
| 7 | Co-doped Mn_3O_4 | 1 M Na_2SO_4 | GCD = 0.5 A g^{-1} | 209 F g^{-1} | [30] |
| 8 | Cu-doped Mn_3O_4 | 1 M Na_2SO_4 | GCD = 0.5 A g^{-1} | 134 F g^{-1} | [30] |
| 9 | Ni-doped Mn_3O_4 | 1 M Na_2SO_4 | GCD = 0.5 A g^{-1} | 184 F g^{-1} | [30] |
| 10 | This work | 1 M Na_2SO_4 | GCD = 1 A g^{-1} | 740 F g^{-1} | — |

drop is a common phenomenon occurring in transition metal oxides. GCDs at various current densities for 0.50 mol% Ni incorporated Mn_3O_4 are presented in Fig. 7b. Specific capacitance (C_{sp}), specific energy (SE), specific power (SP, kW kg^{-1}) and coulomb efficiency (η) are estimated by relations given elsewhere [15]. The specific capacitances obtained from GCD are specified in Table 3. Specific capacitance of 755 F g^{-1} (at 0.5 A g^{-1}) decreased to 708 F g^{-1} (at 4 A g^{-1}), which is more than 230 F g^{-1} stated for the Ni (17.3%)- Mn_3O_4 [50]. Table 4 summarizes the recent research works that were carried out in relation to the doped Mn_3O_4 electrodes including different electrolytes employed. The highest value of 740 F g^{-1} is reported for Ni doped Mn_3O_4 electrodes (Present case). This is followed by 707 F g^{-1} is for Ni doped Mn_3O_4 .

The performance characteristics of Ni doped Mn_3O_4 supercapacitors can be compared with other energy storage systems by plotting the specific energy as a function of specific power on log scale, at different current densities (Ragone plot, Fig. 7c). The

specific energy and specific power are 41.53 Wh kg^{-1} and 1300 W kg^{-1} , respectively. This type of Ni incorporated Mn_3O_4 electrode is beneficial for numerous applications needing high power density and modest energy density. The coulomb efficiency is found to be 95.71%. The results of Ragone plot are given in Table 3.

Long term cycling stability is of huge significance for performance of supercapacitor and is confirmed by GCD cycling (Fig. 7d). It is observed that specific capacitance of Ni incorporated Mn_3O_4 decreases in initial cycles and steady performance during subsequent cycles. After 1000 GCD cycles, the supercapacitor exhibits good cycling life with ~6.38% decrease in specific capacitance. The GCD of the first 10 cycles are revealed in inset of Fig. 7d, which designates the identical symmetric shape, suggesting that the Ni doped Mn_3O_4 electrode does not experience extensive structural changes. The holding of more than 93.62% capacitance after 1000 GCD cycling implies high reversibility of the device.

3.4.3. Electrochemical impedance spectroscopy (EIS)

Fig. 8 (a) shows Nyquist plots for Ni doped Mn_3O_4 electrodes. A semicircle was detected at high and mid frequency for all Ni doped Mn_3O_4 electrodes due to the internal resistance. The ESR of all the Ni doped Mn_3O_4 electrodes is nearly 1 Ω . The EIS data can be fitted by an equivalent circuit shown in Fig. 8 (b) [31]. The elements in the equivalent circuit are solution resistance (R_s), the double-layer capacitance (C_{dl}), the charge-transfer resistance (R_{ct}), the Warburg diffusion element (W_0), and the pseudocapacitance element (C_{pseud}). It is seen that R_{ct} varies with Ni incorporation in Mn_3O_4 . The variation in R_{ct} confirms the dependency Mn_3O_4 electrode on the Ni doping which is related to the difference in crystalline structures [51]. The values of R_s obtained from the Nyquist plots are 0.50 Ω ; 0.35 Ω ; 0.25 Ω ; 0.32 Ω ; and 0.33 Ω respectively for undoped, 0.20 mol %, 0.50 mol %, 0.75 mol %, and 1.00 mol %, Ni incorporated Mn_3O_4 films. The R_{ct} values obtained are 11.70 Ωcm^2 , 10.20 Ωcm^2 , 6.8 Ωcm^2 , 8.25 Ωcm^2 and 10.00 Ωcm^2 for undoped, 0.20 mol %, 0.50 mol %, 0.75 mol %, and 1.00 mol %, Ni incorporated Mn_3O_4 respectively. Among all these, the Mn_3O_4 thin film electrode deposited with 0.50 mol % Ni doping displays a maximum slope which means the most superior capacitive performance. The outstanding capacitive property along with low R_{ct} of Ni doped Mn_3O_4 electrode suggests that it is favorable for excellent electrochemical performance which is good agreement with the CV and GCD results.

4. Conclusion

In this study, doping of nickel into Mn_3O_4 films has been found to upsurge their specific capacitance and improve the surface morphology. The Ni doped Mn_3O_4 are polycrystalline with tetragonal Hausmannite crystal structure. After Nickel doping, the Mn_3O_4 thin film was transformed into highly porous nanoflakes. The optical band gap energy of the Nickel doped Mn_3O_4 electrodes is

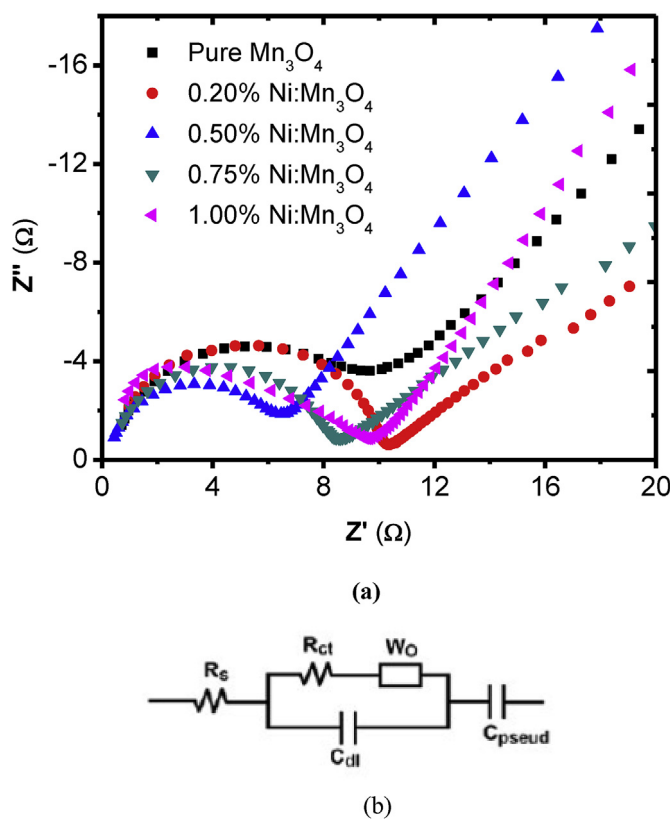


Fig. 8. (a) Nyquist plots for Ni doped Mn_3O_4 thin film electrodes in 1 M Na_2SO_4 electrolyte, and (b) equivalent circuit diagram used for analysis of the EIS data.

2.55–3.29 eV. The nickel doped Mn_3O_4 electrodes exhibit intensive specific capacitance of 705 Fg^{-1} at 10 mVs^{-1} . Specific capacitance calculated at 0.5 Ag^{-1} was 755 Fg^{-1} . The retention of 93.62% specific capacitance after 1000 cycles represents the extraordinary cycling stability of nickel doped Mn_3O_4 electrodes and is greatly analogous to other materials.

References

- [1] Hansa Mahajan, Joonho Bae, Kyusik Yun, Facile synthesis of ZnO -Au nanocomposites for high-performance supercapacitors, *J. Alloys Compd.* 758 (2018) 131–139.
- [2] Jiří Libich, Josef Máca, Jiří Vondrák, Ondřej Čech, Marie Sedláříková, Supercapacitors: properties and applications, *J. Energy Storage* 17 (2018) 224–227.
- [3] Ander González, Eider Goikolea, Jon Andoni Barrena, Roman Mysyk, Review on supercapacitors: technologies and materials, *Renew. Sustain. Energy Rev.* 58 (2016) 1189–1206.
- [4] S. Korkmaz, F. Meydaneri Tezel, I.A. Kariper, Synthesis and characterization of GO/IrO_2 thin film supercapacitor, *J. Alloys Compd.* 754 (2018) 14–25.
- [5] Adrien Mery, Benoît Cagnon, François Tran Van, Cécile Autret, Fouad Ghamouss, Solvent-assisted synthesis of carbon nanotubes-manganese oxide hybrid materials for high voltage aqueous supercapacitor, *J. Alloys Compd.* 763 (2018) 62–70.
- [6] Zhi-Qiang Hou, Feng-Shou Tian, Yong-Ping Gao, Wen Wu, Li-Xia Yang, Xiao-Lu Jia, Ke-Jing Huang, Nickel cobalt hydroxide/reduced graphene oxide/carbon nanotubes for high performance aqueous asymmetric supercapacitors, *J. Alloys Compd.* 753 (2018) 525–531.
- [7] Qing Li, Shasha Zheng, Yuxia Xu, Huaiguo Xue, Huan Pang, Ruthenium based materials as electrode materials for supercapacitors, *Chem. Eng. J.* 333 (2018) 505–518.
- [8] A.A. Yadav, U.J. Chavan, Electrochemical supercapacitive performance of spray deposited Co_3O_4 thin film nanostructures, *Electrochim. Acta* 232 (2017) 370–376.
- [9] Jing Xu, Jiaqiang Li, Qiaoling Yang, Yan Xiong, Changguo Chen, In-situ synthesis of MnO_2 @Graphdiyne oxides nanocomposite with enhanced performance of supercapacitors, *Electrochim. Acta* 251 (2017) 672–680.
- [10] Piaopiao Sun, Zhaojun Li, Lin Zhang, Dong Cui, Zhongjun Li, Hongchang Yao, Jianshe Wang, Guangheng Li, Synthesis of cobalt-nickel pyrophosphates/N-doped graphene composites with high rate capability for asymmetric supercapacitor, *J. Alloys Compd.* 750 (2018) 607–616.
- [11] M. Mondal, B. Das, P. Howli, N.S. Das, K.K. Chattopadhyay, Porosity-tuned NiO nanoflakes: effect of calcination temperature for high performing supercapacitor application, *J. Electroanal. Chem.* 813 (2018) 116–126.
- [12] Chao Feng Liu, Zachary G. Neale, Guozhong Cao, Understanding electrochemical potentials of cathode materials in rechargeable batteries, *Mater. Today* 19 (2016) 109–123.
- [13] M.S. Javed, S. Dai, M. Wang, Y. Xi, Q. Leng, D. Guo, C. Hu, Faradic redox active material of Cu_7S_4 nanowires with high conductance for flexible solid state supercapacitor, *Nanoscale* 7 (2015) 13610–13618.
- [14] L. Ren, J. Chen, X. Wang, M. Zhi, J. Wu, X. Zhang, Facile synthesis of flower-like $CoMn_2O_4$ microspheres for electrochemical supercapacitors, *RSC Adv.* 5 (2015) 30963–30969.
- [15] A.A. Yadav, S.N. Jadhav, D.M. Chougule, P.D. Patil, U.J. Chavan, Y.D. Kolekar, Spray deposited Hausmannite Mn_3O_4 thin films using aqueous/organic solvent mixture for supercapacitor applications, *Electrochim. Acta* 206 (2016) 134–142.
- [16] C.D. Lokhande, D.P. Dubal, Oh-Shim Joo, Metal oxide thin film based supercapacitors, *Curr. Appl. Phys.* 11 (2011) 255–270.
- [17] A.A. Yadav, U.J. Chavan, Electrochemical supercapacitive performance of spray deposited $NiSn_3O_3$ thin films, *Thin Solid Films* 634 (2017) 33–39.
- [18] Xia Yuan, Gang Wang, Xing Zhang, Beibei Wang, Hui Wang, General access to metal oxide (Metal=Mn, Co, Ni) double-layer nanospheres for application in lithium ion batteries and supercapacitors, *Electrochim. Acta* 220 (2016) 643–653.
- [19] R.S. Kate, S.A. Khalate, R.J. Deokate, Overview of nanostructured metal oxides and pure nickel oxide (NiO) electrodes for supercapacitors: a review, *J. Alloys Compd.* 734 (2018) 89–111.
- [20] Yan Zhang, Huijuan Zhang, Ling Fang, Ju Deng, Yu Wang, Facile synthesis of nickel manganese composite oxide nanomesh for efficient oxygen evolution reaction and supercapacitors, *Electrochim. Acta* 245 (2017) 32–40.
- [21] A.A. Yadav, Influence of electrode mass-loading on the properties of spray deposited Mn_3O_4 thin films for electrochemical supercapacitors, *Thin Solid Films* 608 (2016) 88–96.
- [22] Li Ning, Yu Tian, Jianhui Zhao, Jian Zhang, Jun Zhang, Wei Zuo, Yi Ding, Efficient removal of chromium from water by $Mn_3O_4@ZnO/Mn_3O_4$ composite under simulated sunlight irradiation: Synergy of photocatalytic reduction and adsorption, *Appl. Catal. B Environ.* 214 (2017) 126–136.
- [23] Chuen-Chang Lin, Jhang-Hao Jhan, Influence of substrate treatment temperatures and bias potential on capacitive manganese-cobalt-zinc oxide thin films deposited by radio frequency sputtering, *Electrochim. Acta* 56 (2011) 6757–6763.
- [24] Liyuan Cao, Ruiyi Wang, Zhanwei Xu, Jiayin Li, Jianfeng Huang, Ruizi Li, Li Kang, Constructing MnOC bonds in Mn_3O_4 /Super P composite for superior performance in Li-ion battery, *J. Electroanal. Chem.* 798 (2017) 1–8.
- [25] G.S. Gund, D.P. Dubal, B.H. Patil, S.S. Shinde, C.D. Lokhande, Enhanced activity of chemically synthesized hybrid graphene oxide/ Mn_3O_4 composite for high performance supercapacitors, *Electrochim. Acta* 92 (2013) 205–215.
- [26] D.P. Dubal, D.S. Dhawale, R.R. Salunkhe, C.D. Lokhande, A novel chemical synthesis of Mn_3O_4 thin film and its stepwise conversion into birnessite MnO_2 during super capacitive studies, *J. Electroanal. Chem.* 647 (2010) 60–65.
- [27] I. Sheikhshoaei, S. Ramezanpour, M. Khatamian, Synthesis and characterization of thallium doped Mn_3O_4 as superior sunlight photocatalysts, *J. Mol. Liq.* 238 (2017) 248–253.
- [28] Bahareh Ameri, Saeed Hosseiny Davarani, Hamid Reza Moazami, Hamideh Darjazi, Cathodic electrosynthesis of $ZnMn_2O_4/Mn_3O_4$ composite nanostructures for high performance supercapacitor applications, *J. Alloys Compd.* 720 (2017) 408–416.
- [29] Hidayatullah Shah, Fengping Wang, Muhammad Sufyan Javed, Nusrat Shaheen, Muhammad Saleem, Lia Yan, Hydrothermal synthesis of reduced graphene oxide- Mn_3O_4 nanocomposite as an efficient electrode materials for supercapacitors, *Ceram. Int.* 44 (2018) 3580–3584.
- [30] Ruiting Dong, Qinglan Ye, Lili Kuang, Xu Lu, Ying Zhang, Xue Zhang, Guojun Tan, Yanxuan Wen, Fan Wang, Enhanced supercapacitor performance of Mn_3O_4 nanocrystals by doping transition-metal ions, *ACS Appl. Mater. Interfaces* 5 (2013) 9508–9516.
- [31] Yuanzhan Wu, Suqin Liu, Haiyan Wang, Xiwen Wang, Xia Zhang, Guanhua Jin, A novel solvothermal synthesis of Mn_3O_4 /graphene composites for supercapacitors, *Electrochim. Acta* 90 (2013) 210–218.
- [32] T. Larbi, M. Haj Lakhdar, A. Amara, B. Ouni, A. Boukhachem, A. Mater, M. Amlouk, Nickel content effect on the microstructural, optical and electrical properties of p-type Mn_3O_4 sprayed thin films, *J. Alloys Compd.* 626 (2015) 93–101.
- [33] L. Ben Said, K. Juini, F. Hosni, M. Amlouk, Structural and optical investigations on Mn_3O_4 Hausmannite thin films gamma irradiated along with an enhancement of photoluminescence sensing property, *Sensor Actuators Phys.* 271 (2018) 168–173.
- [34] L. Ben Said, A. Inoubli, B. Bouricha, M. Amlouk, High Zr doping effects on the microstructural and optical properties of Mn_3O_4 thin films along with ethanol sensing, *Spectrochim. Acta Mol. Biomol. Spectrosc.* 171 (2017) 487–498.
- [35] U.J. Chavan, A.A. Yadav, Electrochemical behavior of spray deposited mixed nickel manganese oxide thin films for supercapacitor applications, *J. Mater. Sci. Mater. Electron.* 28 (2017) 4958–4964.
- [36] G.M. Biggar, Short communications mineralogical magazine 37 (1969) 286–287.
- [37] A.A. Yadav, M.A. Barote, P.M. Dongre, E.U. Masumdar, Studies on growth and characterization of $CdS_{1-x}Se_x$ ($0.0 \leq x \leq 1.0$) alloy thin films by spray pyrolysis, *J. Alloys Compd.* 493 (2010) 179–185.
- [38] América Vázquez-Olmos, Rocío Redón, Geonel Rodríguez-Gattorno, M. Esther Mata-Zamora, Francisco Morales-Leal, Ana L. Fernández-Osorio, José M. Saniger, One-step synthesis of Mn_3O_4 nanoparticles: structural and magnetic study, *J. Colloid Interface Sci.* 291 (2005) 175–180.
- [39] A.A. Yadav, M.A. Barote, E.U. Masumdar, Studies on cadmium selenide ($CdSe$) thin films deposited by spray pyrolysis, *Mater. Chem. Phys.* 121 (2010) 53–57.
- [40] Binbin Wei, Gui Mei, Hanfeng Liang, Zhengbing Qi, Dongfang Zhang, Hao Shen, Zhoucheng Wang, Porous CrN thin films by selectively etching CrCuN for symmetric supercapacitors, *J. Power Sources* 385 (2018) 39–44.
- [41] Zuxing Mao, Shaobin Zhao, Jing Wang, Yinxiang Zeng, Xihong Lu, Yexiang Tong, Facile synthesis of nitrogen-doped porous carbon as robust electrode for supercapacitors, *Mater. Res. Bull.* 101 (2018) 140–145.
- [42] Lufeng Yang, Shuang Cheng, Ji Xu, Yu Jiang, Jun Zhou, Meilin Liu, Investigations into the origin of pseudocapacitive behavior of Mn_3O_4 electrodes using in operando Raman spectroscopy, *J. Mater. Chem. A* 3 (2015) 7338–7344.
- [43] Imran Khan, Shakeel Khan, Razia Nongjai, Hilal Ahmed, Wasi Khan, Structural and optical properties of gel-combustion synthesized Zr doped ZnO nanoparticles, *Opt. Mater.* 35 (2013) 1189–1193.
- [44] M.A. Amara, T. Larbi, A. Labidi, M. Karyaoui, B. Ouni, M. Amlouk, Microstructural, optical and ethanol sensing properties of sprayed Li-doped Mn_3O_4 thin films, *Mater. Res. Bull.* 75 (2016) 217–223.
- [45] C. Justin Raj, Murugesan Rajesh, Ramu Manikandan, Ju Yong Sim, Kook Hyun Yu, Sang Yeup Park, Jun Ho Song, Byung Chul Kim, Two-dimensional planar supercapacitor based on zinc oxide/manganese oxide Core/Shell nano-architecture, *Electrochim. Acta* 247 (2017) 949–957.
- [46] T.P. Gujar, V.R. Shinde, C.D. Lokhande, Woo-Young Kim, Kwang-Deog Jung, Oh-Shim Joo, Spray deposited amorphous RuO_2 for an effective use in electrochemical supercapacitor, *Electrochim. Commun.* 9 (2007) 504–510.
- [47] Dongwei Li, Fanhui Meng, Xiuling Yan, Lishan Yang, Heng Hua, Ye Zhu, One-pot hydrothermal synthesis of Mn_3O_4 nanorods grown on Ni foam for high performance supercapacitor applications, *Nanoscale Res. Lett.* 8 (2013) 535–542.
- [48] Preety Ahuja, Sanjeev Kumar Ujjain, Rajni Kanodia, Electrochemical behaviour of manganese & ruthenium mixed oxide@ reduced graphene oxide nano-ribbon composite in symmetric and asymmetric supercapacitor, *Appl. Surf. Sci.* 427 (2018) 102–111.
- [49] Jessada Khajornit, Natkrita Prasoetsopha, Tanayt Sinprachim, Pinit Kidkhunthod, Supree Pinitsoontorn, Santi Maensiri, Structure, characterization, and magnetic/electrochemical properties of Ni-doped $BiFeO_3$

- nano-particles, *Adv. Nat. Sci. Nanosci. Nanotechnol.* 8 (12pp) (2017), 015010.
- [50] Guo-rong Xu, Jin-jin Shi, Wen-hao Dong, Ya Wen, Min Xiang-ping, An-ping Tang, One-pot synthesis of a Ni–Mn₃O₄ nanocomposite for supercapacitors, *J. Alloys Compd.* 630 (2015) 266–271.
- [51] Sherdin Khan, Tiago Cassol Severo, Marcos Jose Leite Santos, Sérgio Ribeiro Teixeira, Effect of thermal Calcinations on the charge transfer resistance of tantalum nitride nanotubes, *Nanosci. Nanotechnol.* 6 (2016) 25–28.
- [52] Yufeng Zhao, Wei Ran, Ding-Bang Xiong, Long Zhang, Xu Jiang, Faming Gao, Synthesis of Sn-doped Mn₃O₄/C nanocomposites as supercapacitor electrodes with remarkable capacity retention, *Mater. Lett.* 118 (2014) 80–83.
- [53] Hong-Yan Wang, Deng-Gong Li, Hui-Ling Zhu, Yong-Xin Qi, Hui Li, Lun Ning, Yu-Jun Bai, Mn₃O₄/Ni(OH)₂ nanocomposite as an applicable electrode material for pseudocapacitors, *Electrochim. Acta* 249 (2017) 155–165.
- [54] Hongmei Wei, Jinxing Wang, Yu Le, Yangyang Zhang, Dewen Hou, Tengfei Li, Hydrothermal preparation of nickel-manganese oxide with microsphere structure grown on Ni foam and supercapacitive performance, *Mater. Lett.* 187 (2017) 11–14.
- [55] Chengbao Liu, Hui Sun, Junchao Qian, Zhigang Chen, Feng Chen, Shouqing Liu, Yifei Lv, Xiaowang Lu, Ailian Chen, Ultrafine Mn₃O₄/CeO₂ nanorods grown on reduced graphene oxide sheets as high-performance supercapacitor electrodes, *J. Alloys Compd.* 722 (2017) 54–59.